The Cryosphere

Discussions

EGU

Open Access

Arctic sea ice mass balance in a new coupled ice-ocean model using a brittle rheology framework

Guillaume Boutin[1], Einar Ólason[1], Pierre Rampal[2], Heather Regan[1], Camille Lique[3], Claude Talandier[3], Laurent Brodeau[2], and Robert Ricker[4]

[1]Nansen Environmental and Remote Sensing Center, and the Bjerknes Center for Climate Research, Bergen, Norway
[2]CNRS, Institut de Géophysique de l'Environnement, Grenoble, France
[3]Univ. Brest, CNRS, IRD, Ifremer, Laboratoire d'Océanographie Physique et Spatiale, IUEM, Brest 29280, France
[4]NORCE Norwegian Research Centre, Tromsø, Norway

Correspondence: Guillaume Boutin (guillaume.boutin@nersc.no)

Abstract.

Sea ice is a key component of the Earth's climate system as it modulates the energy exchanges and associated feedback processes at the air-sea interface in polar regions. These exchanges strongly depend on openings in the sea ice cover, which are associated with fine-scale sea ice deformations, but the importance of these processes remains poorly understood as most numerical models struggle to represent these deformations without using very costly horizontal resolutions ($\simeq 2$ km). In this
5 study, we present results from a 12 km resolution ocean–sea-ice coupled model, the first that uses a brittle rheology to represent the mechanical behaviour of sea ice. Using this rheology enables the reproduction of the observed characteristics and complexity of fine-scale sea ice deformations with little dependency on the mesh resolution. We evaluate and discuss the Arctic sea ice mass balance of this coupled model for the period 2000–2018. We first assess sea ice quantities relevant for climate (volume, extent and drift) and find that they are consistent with satellite observations. We evaluate components of the mass
10 balance for which observations are available, i.e. sea ice volume export through Fram Strait and winter mass balance in the Arctic marginal seas for the period 2003–2018. The model performs well, particularly for the dynamic contribution to the winter mass balance. We discuss the relative contributions of dynamics and thermodynamics to the sea ice mass balance in the Arctic Basin for 2000–2018. Benefitting from the model's ability to reproduce fine-scale sea ice deformations, we estimate
15 that the formation of sea ice in leads and polynyas contributes to 25%–35% of the total ice growth in pack ice from January to March, with a significant increase over 2000–2018. This coupled framework opens up new opportunities to understand and quantify the interplay between small-scale sea ice dynamics and ocean properties.

1   Introduction

20   Arctic sea ice is a key component of the global climate system that has been undergoing rapid changes during recent decades (IPCC, Meredith et al., 2019). Its evolution is driven both by thermodynamics (ice growth and melt) and dynamics (ice fracturing, divergence and convergence). At small scales and in the ice pack, sea ice dynamics are characterised by the occurrence of fractures and the formation of ridges and leads, resulting in velocity discontinuities usually referred to as Linear Kinematic Features (LKFs, Kwok et al., 1998). These ubiquitous features, particularly leads, are expected to have a strong impact on

25   ocean-ice-atmosphere interactions in polar regions (Lüpkes et al., 2008; Marcq and Weiss, 2012; Steiner et al., 2013). To fully capture the processes affecting the evolution of sea ice and the effects of the rapid changes taking place in the Arctic, numerical models need to represent the heterogeneity associated with LKFs in the ice cover, and therefore ensure a correct simulation of small-scale ice dynamics.

The reproduction of the observed sea ice cover heterogeneity in models remains a challenge (Blockley et al., 2020; Hunke

30   et al., 2020; Hutter et al., 2021), unless they use horizontal resolutions higher than $\simeq 2$ km (Bouchat et al., 2022; Hutter et al., 2021). Using such a high-resolution grid is very costly and therefore not always suitable for simulations over long periods and/or large domains. LKFs are related to the mechanical behaviour of the sea ice, and their absence in models may therefore be linked to a misrepresentation of this behaviour by the rheologies used in these models (Girard et al., 2009), which are generally using a visco-plastic (VP) framework (Hibler III, 1979). Recent efforts have focused on finding the best

35   way to represent LKFs within a VP rheology framework (e.g. Mehlmann et al., 2021; Ringeisen et al., 2021). An alternative approach would be to use a brittle rheology framework, which has been shown to successfully reproduce LKFs regardless of the horizontal resolution used (Rampal et al., 2019).

Brittle rheologies are relatively new in sea ice modelling, and significant progress has recently been made (Girard et al., 2011; Bouillon and Rampal, 2015; Dansereau et al., 2016; Olason et al., 2021a; Plante and Tremblay, 2021), enabling their use in

40   pan-Arctic process studies (Rampal et al., 2016, 2019; Ólason et al., 2021b; Rheinlænder et al., 2022). However, most of these studies have focused on sea ice deformations and periods of time equal to or shorter than a year. Using a stand-alone version of the *neXt generation Sea Ice Model* (neXtSIM) with the Brittle-Bingham-Maxwell (BBM) rheology, Olason et al. (2021a) were able to reproduce the evolution of Arctic sea ice volume over two decades as well as important statistical characteristics of sea ice deformations. However, the impact of using such a rheology in a large-scale model on the Arctic sea ice mass balance has

45   not yet been assessed.

A modification of the internal stress (the quantity related to the sea ice rheology in the momentum equation) will likely have an impact on the modelled sea ice mass balance in the Arctic (Steele et al., 1997). Changing the internal stress affects large-scale sea ice motion, which impacts the net transport of ice between regions. This net transport has an impact in the regional mass balance that can be comparable to the thermodynamics (Ricker et al., 2021). The importance of the internal stress in

50   controlling the large scale pattern of ice thickness and in the modulation of the ice export through Fram Strait has also been shown in a study by Spall (2019), using scale analysis and an idealized model. Spall (2019) also stresses the close interplay between sea ice dynamics and thermodynamics at large scales.

The Cryosphere
Discussions
Open Access
EGU

Fine-scale sea-ice dynamics also impact the sea ice mass balance. Divergent features in the ice, like leads and polynyas, are associated with localised intense ocean heat loss that enhances sea ice production in winter (Kwok, 2006; Wilchinsky et al., 2015; von Albedyll et al., 2022). The magnitude of ice production in leads remains largely uncertain. Kwok (2006) have estimated this contribution to ≃30% of the total ice production in pack ice from November to April in the western part of the Arctic Basin for the period 1997–2000. More recently, von Albedyll et al. (2022) also estimated this contribution to be around 30% during the Multidisciplinary drifting Observatory for the Study of Arctic Climate (MOSAiC) campaign. These estimates suggest that properly representing ice formation in leads is key to ensuring a realistic magnitude and distribution of ice growth in numerical models. In return, sea ice models that are able to capture such features can assess the importance of leads for ice formation at large scales and over long periods of time, complementing observations when they are missing.

In this study, we investigate the Arctic sea ice mass balance from 2000 to 2018 in a new ocean–sea ice coupled system which uses the ocean component of the Nucleus for European Modelling of the Ocean (NEMO) system and the latest version of the neXtSIM (v2, Olason et al., 2021a). This is the first ocean–sea-ice coupled platform that includes a sea ice model with a brittle rheology. The main objective of this study is to use a coupled ice-ocean modelling system to examine the ice mass balance in the Arctic over the period 2000–2018, and assess the relative importance of the different source and sink terms of that balance in this rheological framework. After a description of the modelling setup, we evaluate the simulated sea ice volume, extent and drift against available observations, as well as the dynamic and thermodynamic contributions to the winter ice mass balance estimated by Ricker et al. (2021) and the sea ice transport through Fram Strait. We then discuss the Arctic mass balance for the whole study period, with a focus on the impact of openings associated with small-scale dynamics (leads and polynyas) in winter.

2 Description of the new coupled sea ice—ocean model

2.1 Model components

The ocean model is OPA, which is part of the NEMO3.6 modelling platform (Madec, 2008). We make use the regional CREG025 configuration (Talandier and Lique, 2021), which is a regional extraction of the global ORCA025 configuration developed by the Drakkar consortium (Barnier et al., 2006). It encompasses the Arctic and parts of the North Atlantic down to 27°, and has 75 vertical levels and a nominal horizontal resolution of $1/4^o (\simeq 12$ km in the Arctic basin). Initial conditions for the ocean are taken from the World Ocean Atlas 2009 climatology for temperature and salinity. For the lateral open boundaries, monthly climatological conditions (comprising sea surface height, 3-D velocities, temperature and salinity) are taken from a long ORCA025 simulation performed by the Drakkar Group.

The sea ice model is the version 2 of the neXtSIM model as recently presented in Olason et al. (2021a). It uses the Brittle-Bingham-Maxwell (BBM) rheology to represent sea ice dynamics. Sea ice thermodynamics are the same as described in appendix A2 of Rampal et al. (2019). In short, neXtSIM considers three ice categories: "thick" ice, open water, and newly formed "young" ice. The young ice is made of ice formed from the super-cooling of open water: this ice category is associated

with Marginal Ice Zones (MIZs) and openings in the ice cover (leads and polynyas). This scheme is used to represent the rapid growth of newly formed ice (young ice, frazil, nylas, etc.), from a minimum thickness $h_{\min}$, set to 5cm, to a maximum thickness $h_{\max}$, that corresponds to the transition to thicker, consolidated ice. Young ice is redistributed in the "thick" ice category once its thickness exceeds $h_{\max}$. Increasing $h_{\max}$ enhances ice growth in the winter. We found that a value of $h_{\max}$=18 cm gives a

90 reasonable winter sea ice thickness in our simulation (see section 4.1). The source and sink terms from the thermodynamics are computed by applying the zero-layer Semtner (1976) vertical thermodynamics to the young ice category and that of Winton (2000) for the thick ice.

The use of a coupled system has required some changes to the default values of the sea ice parameters that were used for simulations using neXtSIM in its stand-alone configuration (as in Rampal et al., 2019; Olason et al., 2021a). These changes

95 are summarised in Table 1. For the dynamics, our setup is very similar to the one described in Olason et al. (2021a), with the exception of small changes in the values of the ice-ocean and ice-atmosphere drag coefficients and a decrease of the value of the scaling parameter for the ridging threshold, P. These changes are needed to ensure that the ice–ocean and ice–atmosphere stresses are properly balanced against the internal ice strength, since this balance is different when neXtSIM is coupled compared to a stand-alone setup. The stress values are chosen to match the observed large scale drift and thickness

100 distribution as well as possible, while still maintaining good deformation patterns and statistics. We use the ice grounding scheme from Lemieux et al. (2015) to represent landfast ice (as in Rampal et al., 2016), with a critical thickness parameter for ice grounding of $k_1 = 5$ (see Lemieux et al., 2015). The initial fields of sea ice thickness and concentration are taken from the same long ORCA025 simulation as used for the ocean lateral boundaries and climatological conditions.

2.2 Coupling between the Lagrangian sea ice and the Eulerian ocean models

105 OPA and neXtSIM are coupled via the OASIS-MCT coupler (Craig et al., 2017). The coupling time step is taken to be equal to the ocean model time step (twice the ice model time step) of 900 s. As summarised in Figure 1, OPA receives all the required information about surface fluxes (heat and salt) and stresses from neXtSIM. In return, OPA sends back information about properties of the ocean surface to neXtSIM. This includes sea surface temperature, salinity, height, and currents, as well as the absorbed fraction of net solar radiation. NEMO includes a coupling interface to run the component model OPA and an

110 ice model (LIM3, SI^3, or CICE) coupled through OASIS. We make use of this coupling interface here, albeit with the minor modifications required to allow for vector orientation on the ocean and ice model grids to be different (as is implicitly assumed in the NEMO code).

One of neXtSIM's particularities is that it uses a Lagrangian moving mesh (Rampal et al., 2016). This ensures little numerical diffusion, which is a condition required to obtain a good localisation of sea ice deformations. However, this particularity

115 makes the interface between neXtSIM and OASIS more complex than a standard coupling interface, as OASIS is not able to accommodate a moving mesh. Therefore, we chose to implement a fixed exchange grid within neXtSIM, which we use to interface with OASIS. For this exchange, neXtSIM interpolates all coupling quantities between the moving mesh and the exchange grid internally, while all communications with OASIS are carried out on the exchange grid (Figure 1). This interpolation is

done by averaging exchanged quantities weighted by the area of overlap between triangles of the mesh and quadrangles of the
120 exchange grid, in a conserving way.

Heat fluxes between the ocean, ice, and atmosphere are computed using traditional bulk formulae. For ocean-atmosphere exchanges, bulk formulae from OPA have been implemented in neXtSIM. This was done using the AeroBulk library (Brodeau et al., 2017), on which OPA has relied since version 4. The bulk formulae for atmosphere-ice fluxes are described in Rampal et al. (2016, 2019). The bulk formulae for ice-ocean fluxes are the same as in the Louvain-La-Neuve sea Ice Model (LIM)
125 version 3.6 (Rousset et al., 2015).

2.3   The Arctic simulation and regions studied

The model simulation, hereafter referred to as OPA-neX, starts on 1st January 1995 and runs until 31st December 2018. Atmospheric forcings are taken from the hourly, 1/4 degree horizontal resolution, ERA5 reanalysis (Hersbach et al., 2020). We exclude the first 5 years of the simulation from the analysis to account for model spin-up. To estimate the length of the
130 spin-up, we applied different initial ice conditions on 1st January 1995, and found no sensitivity of our results over the period 2000–2018 . All output variables from neXtSIM are interpolated using a conservative scheme from the moving Lagrangian model mesh onto a fixed and regular Eulerian grid and are averaged on a 6-hourly basis.

Our analysis focuses on sea ice properties in the Arctic region (Figure 2) where sea ice deformations in neXtSIM have been evaluated before (for instance in Olason et al., 2021a). We divide the Arctic region into 8 sub-domains. The first 6 are similar
135 to those considered in Ricker et al. (2021) (corresponding to the Barents, Kara, Laptev, East Siberian, Chukchi and Beaufort seas). We also consider 2 additional regions that are the Eastern and Western sectors of the Central Arctic (the sub-domains labelled 7 and 8 in Figure 2, respectively). The Eastern sector is typically covered by first year ice being advected towards Fram Strait following the Transpolar Drift, while the Western sector is mostly covered by multiyear ice, generally thicker (>2m) and less mobile than the ice present in the Eastern sector.

140 # 3   Observations used for model evaluation

3.1   Sea ice concentration, volume and drift

We take sea ice concentration from the climate data record of the EUMETSAT Ocean and Sea Ice Satellite Application Facility (OSI-SAF, Lavergne et al., 2019). To cover the period 2000–2018, we use two different versions of the product: the OSI-450 (1980–2015), and the OSI-430-b (2016-present). Sea ice volume and thickness are evaluated using two independent datasets:
145 outputs from the Pan-Arctic Ice-Ocean Modeling and Assimilation System (PIOMAS, Zhang and Rothrock, 2003) and data produced by combining the observations retrieved from the CryoSAT-2 and SMOS satellites, referred to as CS2SMOS (version 2.2, Ricker et al., 2017). The main interest of the PIOMAS dataset is that it is available for the whole simulated period and has been thoroughly evaluated against ice thickness observations (e.g. Schweiger et al., 2011; Laxon et al., 2013; Stroeve et al., 2014). For this reason, it is regularly used as a reference for large-scale sea ice thickness evolution in the Arctic (e.g. Spreen

150 et al., 2020; Davy and Outten, 2020). For evaluating the sea ice drift, we use the low-resolution OSI-SAF sea ice drift product that provides 2-day integrated sea ice displacement (Lavergne et al., 2010). This product includes information about summer ice drift and the uncertainties associated with the drift retrieval from June 2017 onwards.

For each dataset, we process OPA-nex output in order to compare them with observations in a consistent way. First, we integrate in time the 6-hourly OPA-nex output to obtain an output with the same time frequency as the observations (i.e. daily

155 for sea ice concentration, 2-days displacement for the drift, and weekly for the thickness/volume in CS2SMOS). We then interpolate OPA-nex outputs onto the same grid as the observations. There is an additional step for the ice thickness/volume: as PIOMAS is only available monthly, we do a monthly average of OPA-nex outputs and CS2SMOS data, and compare the three datasets with PIOMAS data interpolated on the CS2SMOS 25 km grid.

3.2 Sea ice volume and area export through Fram Strait

160 We also evaluate the ice volume export through Fram Strait, as it is an important contributor to the Arctic sea ice mass balance (Spreen et al., 2009; Ricker et al., 2017; Spreen et al., 2020). We use the time series produced by Spreen et al. (2020), which covers the period 1992–2014, overlapping with most of our simulation. This dataset is based on sea ice thickness measurements derived from 1-4 upward looking sonar measurements installed on moorings across the strait (Vinje et al., 1998) (from which the section of ice thickness is extrapolated), and sea ice drift retrieved from the JPL sea ice motion dataset (Kwok et al.,

165 1998). We also compare OPA-nex results with the time series of Spreen et al. (2009), spanning 2003–2009, that is obtained by combining sea ice thickness from ICESat altimeter observations and sea ice area and drift retrieved from AMSR-E 89 GHz. To compare our export to these datasets in a consistent way, we first estimate the sea ice transport (i.e. motion vectors) at the output frequency of OPA-nex (6h), then interpolate these transports onto the same grid as Spreen et al. (2020). The gate used for the computation is located at $\simeq 79^o$N (see Figure 2).

170 We also compare the simulated sea ice area flux through Fram Strait to the time series estimated by Smedsrud et al. (2017). They combined a blended historical and modern record of sea ice concentration from the National Snow and Ice Data Center (NSIDC, Walsh et al., 2017) with sea level pressure observations across Fram Strait to retrieve the sea ice area flux over the period 1935–2015. Based on the 6-hourly sea ice drift and concentration outputs from OPA-nex, we estimate a time series of the sea ice area flux across the same section at 79^oN (see Figure 2).

175 3.3 Observed contributions to sea ice mass balance

In order to evaluate the ice mass balance and its spatio-temporal variations, we make use of the ice volume change dataset from Ricker et al. (2021). The originality of this dataset is that it separates the dynamic contribution (i.e. the import/export of ice in each region) from the thermodynamic contribution (i.e. the net sea ice growth in winter) to ice volume change in the freezing season (November to March) for 6 Arctic seas (Barents, Kara, Laptev, East Siberian, Chukchi and Beaufort, see Figure 2).

180 To estimate these contributions, Ricker et al. (2021) combine sea ice volume (Hendricks et al., 2018) and motion information (Girard-Ardhuin and Ezraty, 2012) to retrieve the dynamic volume change, and then subtract it from the total volume change to estimate the net sea ice growth. Ricker et al. (2021) also compare their estimations with outputs from 2 models, PIOMAS

and NAOSIM (Kauker et al., 2003). In OPA-nex, we compute the dynamic volume changes in each region from the transports across the gates shown in Figure 2. Thermodynamic volume changes are directly output from the model.

185 **4   Model evaluation**

As stressed in the introduction, the internal stress is an important term in the Arctic mass balance, and it is the first time the mass balance of a sea ice model with a brittle rheology is investigated in detail and over a time period longer than a year. This is also the first time such a model is coupled to an ocean, adding a degree of freedom to the simulation. This section therefore focuses on a careful evaluation of sea ice properties in our simulation to verify that a reasonable Arctic sea ice mass balance is

190 obtained.

4.1   Evaluation of simulated sea ice extent, thickness, volume and drift

We first evaluate the large-scale properties of the simulated sea ice. Our computations of bias, RMSE and integrated ice-edge error (IIEE, Goessling et al., 2016) are done in a similar way to Williams et al. (2021) (section 4.1). The evaluation of small-scale dynamics in neXtSIM (in a standalone setup) is presented in detail in Olason et al. (2021a), and we find no qualitative

195 difference in sea ice deformations with the results from Olason et al. (2021a) after coupling neXtSIM to OPA.

Simulated sea ice extent agrees very well with the OSI-SAF data over the study domain (Figure 3). Importantly, OPA-nex successfully captures the seasonal cycle of the ice extent, and its interannual variability, particularly in the summer, with the exception of 2016 and 2017 where the ice loss is overestimated. We also look at the integrated ice-edge error (IIEE), a metric used to evaluate the quality of predicted ice extent that accounts for both errors in the absolute extent and misplacement of

200 ice (Goessling et al., 2016). The IIEE in our study domain is almost zero in winter (December to May), mostly because we limit our analysis to the Arctic Basin, which is fully ice covered in those months. If we extend our analysis to the whole model domain (that also includes most of the North Atlantic, the Hudson Bay and the Baltic Sea, but not the Pacific side), the modelled sea ice extent remains consistent with observations over the winter. The IIEE remains low (0.62M km^2 in average in March) and almost constant over this season, with a small tendency of the model to underestimate the maximum extent. The

205 IIEE increases in summer and peaks in September (1.7M km^2 in average for this month), mostly due to misplacement of the summer minimum extent (as the absolute value of the extent is generally well estimated, with the exception of 2016 and 2017).

We then examine sea ice volume (Figure 4a). Agreement with PIOMAS is generally good, although sea ice volume in OPA-nex is generally lower than in PIOMAS in the early 2000s. After 2008, the agreement becomes very good in both winter and summer, and the two models show a similar interannual variability. OPA-nex agrees well with CS2SMOS, with an average

210 RMSE of 0.34m and an average bias of 0.03m for the whole period when observations are available (from October to April each year from 2011). This is also true for the ice thickness distribution during the ice growth season (Figure 4b,c,d). Biases in the distribution in OPA-nex compared to CS2SMOS are quite similar to those in PIOMAS and also found in most sea ice models: thick ice is not as thick as the observations in the Central Arctic, and thin ice is often too thick, particularly in the western side of the Arctic Basin (Stroeve et al., 2014; Watts et al., 2021).

7

215   Our simulated drift shows a remarkable agreement with the OSI-SAF data (Figure 5). For the freezing season (October to April), when most of the data are available, OPA-nex shows a low negative bias (-0.35 km/day on average from 2010 to 2018) and a low RMSE (3.82 km/day). OPA-nex also captures both seasonal and interannual variability (Figure 5a) and the day-to-day variability (Figure 5b). Uncertainty and drift estimates in the summer only start in June 2017, hence our choice of zooming in on the year 2018 in Figure 5b. From Figure 5b, modelled summer ice drift is overestimated in OPA-nex compared

220 to OSI-SAF, but remains within the larger uncertainties of observations during the melting season. Importantly, the variability remains well-captured all year round.

4.1.1   Sea ice export through Fram Strait

Sea ice volume export through Fram Strait is an important component of the Arctic sea ice mass balance. Observations suggest $\simeq 13\%$ of the total ice volume in the Arctic Ocean is exported through Fram Strait each year (Spreen et al., 2009; Ricker et al.,

225 2018; Spreen et al., 2020), representing more than 90% of the total sea ice export out of the Arctic (Haine et al., 2015). Figure 6a shows that OPA-nex captures the observed export well as it remains within the standard deviation based on daily transport values estimated by Spreen et al. (2020) over the studied period. However, the model tends to underestimate the magnitude of the export, particularly before 2008. The variability of the export is captured generally well, with a detrended determination coefficient of $R^2 = 0.60$. Again the model seems to perform better after 2008 ($R^2 = 0.70$). The underestimation of the sea ice

230 export before 2008 has an important consequence when we look at the sea ice export trend: while Spreen et al. (2020) find a decreasing trend in the export, we find no significant trend in OPA-nex. It is therefore interesting to investigate the reason behind this discrepancy.

    Sea ice export depends on 3 quantities: thickness, velocity, and concentration across the section. We first examine these two latter quantities by comparing the sea ice area flux in OPA-nex to the time series from Smedsrud et al. (2017) over the period

235 2000–2015 (Figure 6b). We find that OPA-nex agree very well with their estimate, both for the magnitude and variability ($R^2 = 0.81$), which suggests that the model successfully reproduces both the extent of ice in Fram Strait and the ice drift over this period. The discrepancy between our export and the one from Spreen et al. (2020) therefore likely comes from a difference in sea ice thickness across the section, hinting that OPA-nex does not get thick enough ice in the Fram Strait prior to 2008, which is a typical bias in sea ice models (Watts et al., 2021). We note that OPA-nex shows a better agreement with

240 the observations of Spreen et al. (2009), which highlights the uncertainties associated with methods used to retrieve the ice thickness along the section. Sea ice export in 2005–2006, however, remains underestimated in OPA-nex. This, and the fact that the ice volume in OPA-nex for this period is in general lower compared to the PIOMAS model (Figure 4a) suggests OPA-nex sometimes underestimates sea ice thickness over the period 2002–2008.

4.1.2   Regional winter ice mass balance

245 We first investigate the dynamic component of the ice mass balance (the net balance between import and export of sea ice) within the Arctic Basin, in a similar way to Figure 3a of Ricker et al. (2021). The ice transport contribution to the mass balance for the regions where data is available is very well estimated in OPA-nex (Figure 7). The variability is well captured, with

determination coefficients generally exceeding 0.50 between the detrended OPA-nex results and estimations from observations. Similarly to Ricker et al. (2021), we do not find any significant trend over the period 2002–2018 (note that they also include

250   2019 in their study) for any of the regions analysed here. This is also true for the Central Arctic regions (West and East) that are not included in Ricker et al. (2021).

Figure 8 shows the same analysis but for thermodynamic processes, comparable to Figure 3b of Ricker et al. (2021). The thermodynamic processes included in OPA-nex are the production and growth of young ice, the basal growth of (thicker) ice, and ice formed due to the flooding of snow, as well as basal and surface melt. The magnitude of the net winter growth is

255   estimated well in general. The main discrepancies between OPA-nex and Ricker et al. (2021) are found in the Kara and East Siberian seas, where OPA-nex overestimates the amount of ice formed every winter. This is consistent with the behaviour of PIOMAS, shown as a reference in Ricker et al. (2021). As in Ricker et al. (2021), we find a small but significant decreasing trend in ice production in the Kara Sea. Yet, in contrast to their study, we do not find any significant increase in the Chukchi Sea. All other regions are found to have insignificant trends in both OPA-nex and estimations by Ricker et al. (2021). Interannual

260   variability of the net ice growth in each region is generally significantly smaller than the one of the net transport (by a factor $\simeq 2$ for regions 5 to 8), and is not well captured by OPA-nex.

The comparison with Ricker et al. (2021) suggests that the ice mass balance in OPA-nex is captured well in winter. In the next section, we look at the Arctic sea ice mass balance but this time for the whole Arctic Basin, without limiting ourselves to periods covered by observations. This allows us to explore more deeply the links between the dynamic and thermodynamic

265   contributions to the Arctic mass balance.

5 Arctic sea ice mass balance

5.1 Contributions of thermodynamic and dynamic processes

We quantify the contribution of each source and sink of sea ice over time in the domain of interest (Figure 2) for the whole study period (Figure 9a,b). As in section 4.1.2, we partition the sources and sinks of sea ice into dynamic and thermodynamic

270   processes. The dynamic processes are sea ice transport through Fram Strait (in green) and the sum of ice transport through all the other external boundaries of the domain (Figure 2). The thermodynamic processes are the same as in Figure 8. This way of presenting the mass balance is similar to what Keen et al. (2021) have done for sea ice components of climate models that are part of the latest Coupled Model Intercomparison Project (CMIP6). The only difference is that the process we call "growth of young ice" includes both the ice volume of frazil ice production and the ice volume corresponding to the growth of this frazil

275   ice until it enters the consolidated thicker ice category, which occurs when the thickness of the young ice exceeds h_{max} (see section 2.1 for details). This definition of young ice is broadly similar to the one of the World Meteorological Organization (forming ice thinner than 30 cm, WMO, 2014).

We find that the interannual variability of the net mass balance in our domain is controlled by both thermodynamics and the export through Fram Strait, these two terms being of similar amplitude (Figure 9a and Figure 10). Sea ice transport through

280   other gates is negligible compared to the export through Fram Strait (hence almost not visible in Figure 9a,b). In contrast,

when considering the seasonal cycle, sea ice export only plays a minor role in the variations of the ice volume, which are mostly driven by sea ice thermodynamics (Figure 9b). We note that this seasonal cycle is very similar to the multi-model mean seasonal cycle presented in Keen et al. (2021) (see their Figure 4a) even though the framework (fully-coupled climate models, 1960–1989 climatology) is different.

285   Sea ice production slightly exceeds melt in the domain (with the exception of 2016, when the net ice production becomes negative; Figure 9a and Figure 10). This is because we have excluded the domain south of Fram Strait, where a large part of the melting occurs (Figure 9d). The yearly amount of ice growth in the domain is closely linked to the amount of melt (Figure 9a), as the ratio of ice volume growth over melt per year in the study domain is constant over the studied period (not shown). This is most likely because strong melt events lead to large areas of open water and thinner ice at the end of the summer, enhancing

290 the refreezing in the next autumn and winter (Petty et al., 2018). In turn, a positive anomaly in the amount of ice production increases the reservoir of ice that can be melted during the following summer.

    Overall, interannual variations of the net volume change associated with thermodynamic processes are mostly due to variations in the basal growth of thick ice and basal and surface melt (Figure 9a). Basal and surface melt contribute about equally to the yearly ice melt in the domain, while the basal melt strongly dominates south of Fram Strait (outside the study do-

295 main) where sea ice encounters warmer surface waters in the Greenland Sea. Young ice growth accounts for about half of the yearly ice production. This proportion is sensitive to the choice of minimum and maximum thickness for the young ice in our 3-category thermodynamics scheme in OPA-nex (2.1), as is the case in most models (Keen et al., 2021). Young ice growth variability is weaker than that of basal growth, and is mostly controlled by two drivers: the ice extent at the end of the summer (positive anomalies are found in e.g. 2008, 2013 or 2017, which are years following low-extent anomalies), and the amount of

300 openings (leads or polynyas) that are present in pack ice. Ice production due to the flooding of snow is negligible for the area and time period discussed in this analysis. The ice volume loss over time in the domain is clearly visible in Figure 10. This loss is qualitatively similar to the winter volume evolution reported by Liu et al. (2020) using ice age to estimate the ice volume. We find a trend of -170 km^3 per year over 2000–2018, which compares reasonably well with the trends in sea ice volume (from both models and observations) discussed in Liu et al. (2020). The comparable orders of magnitude of the ice exported and the

305 net change in ice volume due to thermodynamics reinforce the importance of the dynamic contribution to the mass balance that was suggested in Figure 9. Net ice production peaks in 2013–14, when it dominates the net export by a factor of $\simeq 2$, resulting in an increase of the ice volume in the domain. Loss of sea ice volume in the domain mostly occurs in years of low (or negative) net ice production (such as 2002, 2012 and 2016). The yearly net sea ice export varies very little in comparison to the net sea ice production.

310 ## 5.2   Contributions of leads and coastal polynyas to winter ice production

We now use neXtSIM's capability to reproduce small-scale sea ice dynamics, and particularly its ability to simulate rates of divergence consistent with observations (Olason et al., 2021a), to assess the importance of spatial heterogeneity in the ice cover to winter (January to March) ice growth. To do this, we assume that, in winter, the formation and growth of young ice is related to the presence of leads and polynyas. Young ice is associated with ice growth in open water, MIZs, and openings in pack ice

315   (see section 2.1). In coastal areas, the expression "openings in pack ice" can correspond to both leads and polynyas, while in regions away from the shelves it mainly corresponds to leads.

    The impact of heterogeneity of the sea ice cover on winter ice production is visible in Figure 11a, and is clearly linked to the growth of young ice (Figure 11b). We note that the spatial patterns in Figure 11a,b look similar to maps of observed ice divergence or lead fraction distribution described in previous studies (e.g. Kwok, 2006; Willmes and Heinemann, 2016; Wang

320   et al., 2016; Zhang et al., 2018). The imprint of leads on ice production is particularly visible in the Beaufort Sea, with long linear features orthogonal to the coast. Their presence in a 18-year long climatology demonstrates their strong impact on sea ice production and the likely recurrence of these features year after year. Lead-type features are also visible in the Central Arctic when looking at the contribution of openings to the total growth (Figure 11b). This is likely because the thick ice covering the Central Arctic limits the amount of ocean heat loss, hence basal growth, that can occur, meaning that local openings in

325   this thick ice cover significantly contribute to the total ice growth there. We also note that coastal areas are places of intense production of newly formed ice in winter, likely due to the recurrent opening of coastal polynyas.

    Before quantifying the impact of leads and polynyas to winter ice production, we assess the limitations of associating the growth of young ice with these types of features. From Figure 11c, we can differentiate 2 phases in ice growth within the freezing season. The first period (October to December) is when ice production is dominated by the growth of young ice from

330   open water, as the open water refreezes. Young ice growth occurs in open water areas in a homogeneous way until the whole Arctic Basin is ice covered. The second phase is from January to March, when the contributions of basal growth and young ice growth reach an equilibrium. This corresponds to a plateau in the contribution of the growth of young ice to total growth, visible every year in Figure 11c. Sea ice concentrations in the domain are then very close to 100% everywhere, which means that the young ice is mostly (if not totally) produced from openings due to divergence in pack ice (Strong and Rigor, 2013).

335   There are, however, regions in our domain that remain covered with thin ice in winter, or even include open water areas (e.g the Barents Sea). To avoid the inclusion of young ice production in MIZs in our analysis, we remove the southern part of the Chukchi Sea, as well as the Barents and Kara seas from the domain we consider (black contour, Figure 11a,b).

    We now quantify the contribution of ice growth due to openings within pack ice over the total ice growth. This contribution adds up to $\simeq$25% to 35% of the ice growth in the domain (black line in Figure 11e). This corresponds to an annual winter ice

340   volume production of $\simeq$270 to 380 km^3 (black line in Figure 11d). We find that young ice growth is increasing over the studied period with a significant (i.e with a p-test result lower than 0.05) positive trend of +74.7 km^3 per decade. This is also true for its contribution to total growth, with a positive trend of + 4.3% per decade. Over the same period, the basal and total growth show no significant trends (not shown).

    As mentioned before, ice growth from leads and polynyas is particularly substantial in coastal areas. It is therefore interesting

345   to distinguish between coastal areas, where both leads and polynyas can occur, from the interior Arctic Basin, where most openings correspond to leads. We reproduce our analysis, excluding this time the regions shallower than 300m (cyan dashed contour in Figure 11,a,b). We find that the interior Arctic basin accounts for about half of the young ice growth from openings in pack ice in winter (grey lines in Figure 11d,e). We still find significant positive trends in young ice growth (+29.4 km^3 per decade) and its contribution to total ice growth. This means that while ice production in leads in the interior Arctic is a

350 significant contributor in the study domain, it is the coastal areas that are most important to the modelled increase in ice growth in leads and polynyas over 2000–2018 (Figure 11d).

We note that most of the increase in the contribution of ice growth in leads and polynyas to total ice growth takes place from 2000 to 2010, with a significant positive trend of about +7% over this decade (whether the shelves are excluded or not). From 2008 to 2018, we find no significant trend for ice growth in leads and polynyas. Using 2018 as the last year of the analysis, the

355 positive trend in the contribution of ice growth in leads and polynyas to total ice growth is only significant when starting prior to 2005 (included), and prior to 2002 if we exclude the shelves. This highlights the important contribution of the earlier years of the analysis (the period from 2000 to 2008 in particular) to this increasing trend in ice production.

5.3 Regional variability and trends in winter ice production in leads/polynyas

To better understand this evolution of ice growth in leads and polynyas, we now look into more detail at each region included

360 in our analysis (Figure 12a-f). Although ice growth in leads and polynyas strongly varies from one region to another (Figure 12a), its contribution to total growth is similar across the subdomains, around 30% if we account for coastal areas, and about 25% when we only consider the interior of the basin (Figure 12e). However, there are two regions where the behaviour differs from the other regions. The contribution is lower in the Western Central Arctic ($\simeq$24% including coastal areas), likely due to thick sea ice, which is not very mobile (Figure 12g,i). Oppositely, the Eastern Central Arctic is characterised by a large

365 contribution of leads and polynyas to sea ice production ($\simeq$44%; $\simeq$39% when excluding the shelves), likely due to the large cracks that regularly form as the ice undergoes high internal stresses while exiting through the narrow Fram Strait (as visible in Figure 11a, and in lead frequency maps in Willmes and Heinemann, 2016). Increases in winter ice volume growth due to leads and polynyas (and their contribution to total growth) occur in almost every region over 2000–2018 (Figure 12b,f), but are only significant in the regions along the Eurasian Coast (Laptev, East Siberian and Chukchi seas), and in the interior of the Chukchi

370 Sea. The largest trends are found in the Laptev and East Siberian seas, as well as in the interior of the Chukchi Sea. Total ice volume growth shows no significant trend anywhere (Figure 12d).

We now try to relate this increase in the ice growth in leads and polynyas to two other sea ice quantities that are related to sea ice deformation: sea ice drift and thickness (Figure 12g-j). Sea ice drift speed is found to increase over time, with positive significant trends varying between +10% to +20% per decade depending on the region (Figure 12h). Spatial variability of sea

375 ice drift trend magnitudes follows that of ice growth in leads and polynyas, which suggests a close relationship between the two. As for the ice growth in leads and polynyas, most of this increase in ice drift speed occurs over the period 2000–2008, there is no significant trend for any region for the period 2008–2018 (not shown). In the case of sea ice thickness, the relationship with ice growth in leads and polynyas is less clear. The thinning trend is significant almost everywhere (Figure 12j), but the spatial distribution of the trend magnitude does not reflect the one of ice growth in leads and polynyas. We note that sea ice

380 drift and thickness are not independent, and the increase in ice drift speed is most likely driven by the thinning of the ice and the associated reduction of the ice strength (Rampal et al., 2009). Similarly to what was found in previous studies (Rampal et al., 2009; Kwok et al., 2013), we find no or very little trend in the wind speed, with magnitudes that are too low to explain the increase in ice drift (not shown).

Our interpretation of the results is that the increasing trend in the ice drift velocity is associated with higher divergence
385   rates, enhancing winter ice production in openings in the ice pack. This feedback has been suggested before. Kwok (2006), for
instance, has hypothesised that it could contribute to the resilience of sea ice in the Arctic. This enhanced winter ice production
is particularly intense close to the coast and in regions with thin ice, such as the Laptev and Siberian seas (Figure 12b,f). These
regions are also associated with rather low average ice drift speed in winter, most likely due to the presence of landfast ice.
Therefore, landfast ice, and the leads and polynyas that form along it, likely play an important role in the production of ice in
390   winter along the Eurasian coast.

6   Discussion

In our analysis, we have highlighted the importance of the contribution of sea ice dynamics to the sea ice mass balance. One
interesting result is our estimation of the winter ice growth that is associated with leads and polynyas. This quantity has, until
now, not been estimated at the pan-Arctic scale due to difficulties in estimating it from observations, particularly on large
395   scales, and the inability of many models to correctly simulate LKFs (Hutter et al., 2021; Bouchat et al., 2022). At first glance,
our estimate that sea ice production in leads contributes to between 25 and 35% of the winter ice production in the Arctic agrees
well with previous estimates from Kwok (2006, $\simeq$25 to 40%) and von Albedyll et al. (2022, $\simeq$30%). However, we acknowledge
that the methods, time periods, and the spatial and temporal scales we use are different to the one used in these two studies. In
the following paragraphs we briefly discuss these values and their context, although a fully consistent comparison with each of
400   these estimates remains outside the scope of this study.

In their study, von Albedyll et al. (2022) estimate that ice production in leads represents about 30% of ice production in
the 2019–2020 freezing season, but they distinguish two periods: from October 2019 to early April 2020, when ice formation
in leads contributes to around 10% of sea ice production, and from April 2020 to June 2020, when most of the ice formation
takes place in leads and the net contribution of basal growth is almost zero. Their estimation gives a Lagrangian view of ice
405   production in pack ice, following the drift of the MOSAiC expedition between the north of the East Siberian Sea to the north
of Svalbard. Their estimate of 10% for the period from October to early April is not very different from our estimate for the
East Siberian Sea when excluding the shelf coast ($\simeq$ 18%, Figure 12e). This is consistent with the fact that a large part of the
vessel drift took place north of 85^oN, where the contribution of leads to winter ice production is rather low (generally $\leq$20%,
Figure 11b). It is also likely that, in autumn, basal growth contribution to ice production in pack ice is larger than from January
410   to March, as level ice and its snow layer are generally thinner, hence allowing for more heat loss from the ocean in ice covered
areas. von Albedyll et al. (2022) suggest that the higher contribution of leads to ice production in spring than in winter could
be partly resulting from regional differences, as the vessel drifted towards regions with a higher contribution of leads to the ice
production. Our model suggests this is likely the case (Figure 11b).

Kwok (2006) investigates the western part of the Arctic Basin over the period 1997–2000, when most of the ice cover was
415   made of multiyear ice. To estimate the quantity of ice that is produced in leads, they combined a thermodynamic model with
sea ice deformations retrieved from the Radarsat Geophysical Processing System (RGPS, Kwok et al., 1998). They used a

rough estimate of the amount of basal and total growth to provide an order of magnitude of the contribution of leads to the total ice production from November to April. In our analysis, we excluded the late autumn (November-December) to avoid including frazil production in MIZs, and focus on young ice growth in pack ice, associated with leads and polynyas. However,

420 in the late 1990s sea ice was already compact in the western part of the Arctic Basin from November onwards. Therefore we can estimate the contribution of leads and polynyas to the ice growth from November 1999 to March 2000 in OPA-nex using the same method as in section 5.3. We find values of 30% for the Western Central Arctic and 35% for the Beaufort Sea (22% and 25% respectively when excluding the shelf area), which is within the range of values estimated in Kwok (2006).

Our estimates of ice growth in leads are mostly sensitive to i) rheological parameters affecting sea ice divergence and ii) the

425 maximum thickness of young ice (h_{max}). In case i), we ensured that our results were consistent with the stand-alone version of neXtSIM presented and evaluated in Olason et al. (2021a), which was found to produce realistic divergence rates. In case ii), we tested h_{max} values in the range [12.5cm, 22.5cm], and found that larger values resulted in overestimated ice thickness, particularly in the Kara and Barents seas. This range of values seems reasonable to represent the transition between forming ice (frazil, pancake, nylas) and consolidated first-year ice.

430 To our knowledge, the increase in both the amount of ice produced in leads and its relative contribution to the winter ice production has not been reported before. Studies focusing on leads in the Arctic often investigate the evolution of the observed lead frequency (Lewis and Hutchings, 2019; Willmes and Heinemann, 2016) or the modelled lead area fraction (Wang et al., 2016; Ólason et al., 2021b). A consistent comparison of the lead frequency between OPA-nex and observations is not straightforward, but it is likely that lead frequency is closely linked to the amount of ice production in leads. Willmes and

435 Heinemann (2016) investigate the evolution of lead frequency in the Arctic over 2003–2015 using thermal infrared imagery. They find that interannual variability is large and there is no significant trend. If we limit our analysis to 2003–2015, we also find no significant trend in the evolution of ice growth in leads and polynyas (Figure 11d). Further analysis of observations and model results is therefore required to further investigate these findings.

7 Conclusions

440 In this study, we have presented a new ocean–sea-ice coupled model and evaluated its representation of the sea ice mass balance over the Arctic region. For the first time in this type of study, the sea ice model uses a brittle rheology to represent the sea ice mechanics. The simulation captures very well the standard sea ice evaluation metrics of sea ice extent and volume, as well as large-scale drift and export through Fram Strait. The winter mass balance is consistent with observations for the period 2003–2018. The ability of the sea ice model to simulate fracturing and the subsequent sea ice deformations is used to

445 assess the contributions of leads and polynyas to the mass balance. We estimate this contribution to be 25% to 35% of winter ice volume growth, in line with previous estimates from Kwok (2006) based on satellite observations. We also find that this contribution has increased over 2000–2018, mostly due to an increase of openings in coastal areas associated with an increase of ice drift velocity. Future studies will focus more precisely on the representation of leads in the model, and compare them to available observations (e.g. Willmes and Heinemann, 2016; Reiser et al., 2020) to assess the nature of this increase. Extending

450   the analysis based on the distinction between leads and pack ice over all seasons could also provide new insights into the importance of small-scale dynamics to the ice mass balance, especially as von Albedyll et al. (2022) noted the importance of ice formation in leads from April to June.

Our results illustrate the interest of using a brittle rheology framework in ice–ocean coupled modelling. This framework is able to capture the spatial and temporal heterogeneity of the ice cover, opening up the possibility to assess how this hetero-

455   geneity affects the ocean surface properties. For instance, it is likely that the reported localised ice growth in the winter has an impact on the mixed-layer properties, for example its heat content. In spring, summer and autumn, the presence of leads also modulates the amount of light entering the ocean and likely affects the ocean's biogeochemistry (Assmy et al., 2017). Using a higher horizontal resolution than in our study would additionally allow the investigation of other expected impacts of leads on the ocean dynamics, such as the generation of submesoscale oceanic eddies as recently presented in Cohanim et al. (2021), as

460   the level of understanding of such coupled processes and interactions is still limited.

References

Assmy, P., Fernández-Méndez, M., Duarte, P., Meyer, A., Randelhoff, A., Mundy, C. J., Olsen, L. M., Kauko, H. M., Bailey, A., Chierici, M., Cohen, L., Doulgeris, A. P., Ehn, J. K., Fransson, A., Gerland, S., Hop, H., Hudson, S. R., Hughes, N., Itkin, P., Johnsen, G., King, J. A., Koch, B. P., Koenig, Z., Kwasniewski, S., Laney, S. R., Nicolaus, M., Pavlov, A. K., Polashenski, C. M., Provost, C., Rösel, A., Sandbu, M., Spreen, G., Smedsrud, L. H., Sundfjord, A., Taskjelle, T., Tatarek, A., Wiktor, J., Wagner, P. M., Wold, A., Steen, H., and Granskog, M. A.: Leads in Arctic pack ice enable early phytoplankton blooms below snow-covered sea ice, Scientific Reports, 7, 40 850, https://doi.org/10.1038/srep40850, 2017.

Barnier, B., Madec, G., Penduff, T., Molines, J.-M., Treguier, A.-M., Sommer, J. L., Beckmann, A., Biastoch, A., Böning, C., Dengg, J., Derval, C., Durand, E., Gulev, S., Remy, E., Talandier, C., Theetten, S., Maltrud, M., McClean, J., and Cuevas, B. D.: Impact of partial steps and momentum advection schemes in a global ocean circulation model at eddy-permitting resolution, Ocean Modelling, 56, 543–567, https://doi.org/10.1007/s10236-006-0082-1, 2006.

Blockley, E., Vancoppenolle, M., Hunke, E., Bitz, C., Feltham, D., Lemieux, J.-F., Losch, M., Maisonnave, E., Notz, D., Rampal, P., Tietsche, S., Tremblay, B., Turner, A., Massonnet, F., Olason, E., Roberts, A., Aksenov, Y., Fichefet, T., Garric, G., Iovino, D., Madec, G., Rousset, C., y Melia, D. S., and Schroeder, D.: The Future of Sea Ice Modeling: Where Do We Go from Here?, Bulletin of the American Meteorological Society, 101, E1304 – E1311, https://doi.org/10.1175/BAMS-D-20-0073.1, 2020.

Bouchat, A., Hutter, N., Chanut, J., Dupont, F., Dukhovskoy, D., Garric, G., Lee, Y. J., Lemieux, J.-F., Lique, C., Losch, M., Maslowski, W., Myers, P. G., Ólason, E., Rampal, P., Rasmussen, T., Talandier, C., Tremblay, B., and Wang, Q.: Sea Ice Rheology Experiment (SIREx): 1. Scaling and Statistical Properties of Sea-Ice Deformation Fields, Journal of Geophysical Research: Oceans, 127, e2021JC017 667, https://doi.org/https://doi.org/10.1029/2021JC017667, e2021JC017667 2021JC017667, 2022.

Bouillon, S. and Rampal, P.: Presentation of the dynamical core of neXtSIM, a new sea ice model, Ocean Modelling, 91, 23–37, https://doi.org/10.1016/j.ocemod.2015.04.005, 2015.

Brodeau, L., Barnier, B., Gulev, S. K., and Woods, C.: Climatologically Significant Effects of Some Approximations in the Bulk Parameterizations of Turbulent Air–Sea Fluxes, Journal of Physical Oceanography, 47, 5–28, https://doi.org/10.1175/JPO-D-16-0169.1, publisher: American Meteorological Society Section: Journal of Physical Oceanography, 2017.

Cohanim, K., Zhao, K. X., and Stewart, A. L.: Dynamics of Eddies Generated by Sea Ice Leads, Journal of Physical Oceanography, 51, 3071 – 3092, https://doi.org/10.1175/JPO-D-20-0169.1, 2021.

Craig, A., Valcke, S., and Coquart, L.: Development and performance of a new version of the OASIS coupler, OASIS3-MCT_3. 0, Geoscientific Model Development, 10, 3297, 2017.

Dansereau, V., Weiss, J., Saramito, P., and Lattes, P.: A Maxwell elasto-brittle rheology for sea ice modelling, The Cryosphere, 10, 1339–1359, 2016.

Davy, R. and Outten, S.: The Arctic Surface Climate in CMIP6: Status and Developments since CMIP5, Journal of Climate, 33, 8047 – 8068, https://doi.org/10.1175/JCLI-D-19-0990.1, 2020.

Girard, L., Weiss, J., Molines, J.-M., Barnier, B., and Bouillon, S.: Evaluation of high-resolution sea ice models on the basis of statistical and scaling properties of Arctic sea ice drift and deformation, Journal of Geophysical Research: Oceans, 114, 2009.

Girard, L., Bouillon, S., Weiss, J., Amitrano, D., Fichefet, T., and Legat, V.: A new modeling framework for sea-ice mechanics based on elasto-brittle rheology, Annals of Glaciology, 52, 123–132, https://doi.org/10.3189/172756411795931499, 2011.

Girard-Ardhuin, F. and Ezraty, R.: Enhanced Arctic sea ice drift estimation merging radiometer and scatterometer data, IEEE Trans. on

510   Geosci. and Remote Sensing, 50, 2639–2648, 2012.

Goessling, H. F., Tietsche, S., Day, J. J., Hawkins, E., and Jung, T.: Predictability of the Arctic sea ice edge, Geophysical Research Letters,
     43, 1642–1650, https://doi.org/https://doi.org/10.1002/2015GL067232, 2016.

Haine, T. W., Curry, B., Gerdes, R., Hansen, E., Karcher, M., Lee, C., Rudels, B., Spreen, G., de Steur, L., Stewart, K. D.,
     and Woodgate, R.: Arctic freshwater export: Status, mechanisms, and prospects, Global and Planetary Change, 125, 13–35,

515   https://doi.org/https://doi.org/10.1016/j.gloplacha.2014.11.013, 2015.

Hendricks, S., Paul, S., and Rinne, E.: ESA Sea Ice Climate Change Initiative (Sea_Ice_cci): Northern hemisphere sea ice thickness from
     the Envisat satellite on a monthly grid (L3C), v2.0, https://doi.org/10.5285/F4C34F4F0F1D4D0DA06D771F6972F180, medium: appli-
     cation/xml Version Number: 3.1 Type: dataset, 2018.

Hersbach, H., Bell, B., Berrisford, P., Hirahara, S., Horányi, A., Muñoz-Sabater, J., Nicolas, J., Peubey, C., Radu, R., Schepers, D., Sim-

520   mons, A., Soci, C., Abdalla, S., Abellan, X., Balsamo, G., Bechtold, P., Biavati, G., Bidlot, J., Bonavita, M., De Chiara, G., Dahlgren,
     P., Dee, D., Diamantakis, M., Dragani, R., Flemming, J., Forbes, R., Fuentes, M., Geer, A., Haimberger, L., Healy, S., Hogan, R. J.,
     Hólm, E., Janisková, M., Keeley, S., Laloyaux, P., Lopez, P., Lupu, C., Radnoti, G., de Rosnay, P., Rozum, I., Vamborg, F., Vil-
     laume, S., and Thépaut, J.-N.: The ERA5 global reanalysis, Quarterly Journal of the Royal Meteorological Society, 146, 1999–2049,
     https://doi.org/https://doi.org/10.1002/qj.3803, 2020.

525 Hibler III, W. D.: A Dynamic Thermodynamic Sea Ice Model, Journal of Physical Oceanography, 9, 815–846, https://doi.org/10.1175/1520-
     0485(1979)009<0815:ADTSIM>2.0.CO;2, 1979.

Hunke, E., Allard, R., Blain, P., Blockley, E., Feltham, D., Fichefet, T., Garric, G., Grumbine, R., Lemieux, J.-F., Rasmussen, T., Ribergaard,
     M., Roberts, A., Schweiger, A., Tietsche, S., Tremblay, B., Vancoppenolle, M., and Zhang, J.: Should Sea-Ice Modeling Tools Designed
     for Climate Research Be Used for Short-Term Forecasting?, Current Climate Change Reports, 6, 121–136, https://doi.org/10.1007/s40641-

530   020-00162-y, 2020.

Hutter, N. C., Bouchat, A., Dupont, F., Dukhovskoy, D. S., Koldunov, N. V., Lee, Y. J., Lemieux, J.-F., Lique, C., Losch, M., Maslowski, W.,
     et al.: Sea Ice Rheology Experiment (SIREx), Part II: Evaluating simulated linear kinematic features in high-resolution sea-ice simulations,
     Earth and Space Science Open Archive ESSOAr, 2021.

Kauker, F., Gerdes, R., Karcher, M., Köberle, C., and Lieser, J. L.: Variability of Arctic and North Atlantic sea ice: A combined analysis of

535   model results and observations from 1978 to 2001, Journal of Geophysical Research: Oceans, 108, 2003.

Keen, A., Blockley, E., Bailey, D. A., Boldingh Debernard, J., Bushuk, M., Delhaye, S., Docquier, D., Feltham, D., Massonnet, F., O'Farrell,
     S., Ponsoni, L., Rodriguez, J. M., Schroeder, D., Swart, N., Toyoda, T., Tsujino, H., Vancoppenolle, M., and Wyser, K.: An inter-
     comparison of the mass budget of the Arctic sea ice in CMIP6 models, The Cryosphere, 15, 951–982, https://doi.org/10.5194/tc-15-
     951-2021, 2021.

540 Kwok, R.: Contrasts in sea ice deformation and production in the Arctic seasonal and perennial ice zones, Journal of Geophysical Research:
     Oceans, 111, https://doi.org/10.1029/2005JC003246, _eprint: https://agupubs.onlinelibrary.wiley.com/doi/pdf/10.1029/2005JC003246,
     2006.

Kwok, R., Schweiger, A., Rothrock, D., Pang, S. S., and Kottmeier, C.: Sea ice motion from satellite passive microwave imagery assessed
     with ERS SAR and buoy motions, J. Geophys. Res., 103, 8191–8214, 1998.

545 Kwok, R., Spreen, G., and Pang, S.: Arctic sea ice circulation and drift speed: Decadal trends and ocean currents, Journal of Geophysical
     Research: Oceans, 118, 2408–2425, https://doi.org/10.1002/jgrc.20191, transpolar Drift, 2013.

Lavergne, T., Eastwood, S., Teffah, Z., Schyberg, H., and Breivik, L.-A.: Sea ice motion from low-resolution satellite sensors: An alternative method and its validation in the Arctic, Journal of Geophysical Research: Oceans, 115, https://doi.org/https://doi.org/10.1029/2009JC005958, 2010.

550 Lavergne, T., Sørensen, A. M., Kern, S., Tonboe, R., Notz, D., Aaboe, S., Bell, L., Dybkjær, G., Eastwood, S., Gabarro, C., Heygster, G., Killie, M. A., Brandt Kreiner, M., Lavelle, J., Saldo, R., Sandven, S., and Pedersen, L. T.: Version 2 of the EUMETSAT OSI SAF and ESA CCI sea-ice concentration climate data records, The Cryosphere, 13, 49–78, https://doi.org/10.5194/tc-13-49-2019, 2019.

Laxon, S. W., Giles, K. A., Ridout, A. L., Wingham, D. J., Willatt, R., Cullen, R., Kwok, R., Schweige, r. A., Zhang, J., Haas, C., Hendricks, S., Krishfield, R., Kurtz, N., Farrell, S., and Davidson, M.: CryoSat-2 estimates of Arctic sea ice thickness and volume, Geophysical

555 Research Letters, 40, 732–737, https://doi.org/10.1002/grl.50193, 2013.

Lemieux, J.-F., Tremblay, L. B., Dupont, F., Plante, M., Smith, G. C., and Dumont, D.: A basal stress parameterization for modeling landfast ice, Journal of Geophysical Research: Oceans, 120, 3157–3173, https://doi.org/https://doi.org/10.1002/2014JC010678, 2015.

Lewis, B. J. and Hutchings, J. K.: Leads and Associated Sea Ice Drift in the Beaufort Sea in Winter, Journal of Geophysical Research: Oceans, 124, 3411–3427, https://doi.org/https://doi.org/10.1029/2018JC014898, 2019.

560 Liu, Y., Key, J. R., Wang, X., and Tschudi, M.: Multidecadal Arctic sea ice thickness and volume derived from ice age, The Cryosphere, 14, 1325–1345, https://doi.org/10.5194/tc-14-1325-2020, 2020.

Lüpkes, C., Vihma, T., Birnbaum, G., and Wacker, U.: Influence of leads in sea ice on the temperature of the atmospheric boundary layer during polar night, Geophysical Research Letters, 35, https://doi.org/https://doi.org/10.1029/2007GL032461, 2008.

Madec, G.: NEMO ocean engine, Note du Pôle de modélisation, Institut Pierre-Simon Laplace (IPSL), France, No 27, ISSN No 1288-1619,

565 2008.

Marcq, S. and Weiss, J.: Influence of sea ice lead-width distribution on turbulent heat transfer between the ocean and the atmosphere, The Cryosphere, Volume 6, Issue 1, 2012, pp. 143-156, 6, 143–156, 2012.

Mehlmann, C., Danilov, S., Losch, M., Lemieux, J. F., Hutter, N., Richter, T., Blain, P., Hunke, E. C., and Korn, P.: Simulating linear kinematic features in viscous-plastic sea ice models on quadrilateral and triangular grids, 2021.

570 Meredith, M., Sommerkorn, M., Cassota, S., Derksen, C., Ekaykin, A., Hollowed, A., Kofinas, G., Mackintosh, A., Melbourne-Thomas, J., Muelbert, M. M. C., Ottersen, G., Pritchard, H., Schuur, E. A. G., Boyd, P., Hobbs, W., and Hodgson-Johnston, I.: Polar Regions, pp. 1–173, IPCC, WMO, UNEP, https://www.ipcc.ch/srocc/home/, 2019.

Olason, E., Boutin, G., Korosov, A., Rampal, P., Williams, T., Kimmritz, M., Dansereau, V., and Samaké, A.: A new brittle rheology and numerical framework for large-scale sea-ice models, ESSOAr, https://doi.org/10.1002/ESSOAR.10507977.1, 2021a.

575 Ólason, E., Rampal, P., and Dansereau, V.: On the statistical properties of sea-ice lead fraction and heat fluxes in the Arctic, The Cryosphere, 15, 1053–1064, https://doi.org/10.5194/tc-15-1053-2021, 2021b.

Petty, A. A., Holland, M. M., Bailey, D. A., and Kurtz, N. T.: Warm Arctic, Increased Winter Sea Ice Growth?, Geophysical Research Letters, 45, 12,922–12,930, https://doi.org/https://doi.org/10.1029/2018GL079223, 2018.

Plante, M. and Tremblay, L. B.: A generalized stress correction scheme for the Maxwell elasto-brittle rheology: impact on the fracture angles

580 and deformations, The Cryosphere, 15, 5623–5638, https://doi.org/10.5194/tc-15-5623-2021, 2021.

Rampal, P., Weiss, J., and Marsan, D.: Positive trend in the mean speed and deformation rate of Arctic sea ice, 1979–2007, Journal of Geophysical Research: Oceans, 114, https://doi.org/https://doi.org/10.1029/2008JC005066, 2009.

Rampal, P., Bouillon, S., Olason, E., and Morlighem, M.: neXtSIM: a new Lagrangian sea ice model, CRYOSPHERE, 10, https://doi.org/10.5194/tc-10-1055-2016, 2016.

585   Rampal, P., Dansereau, V., Ólason, E., Bouillon, S., Williams, T., Korosov, A., and Samaké, A.: On the multi-fractal scaling properties of sea ice deformation, The Cryosphere, 13, 2457–2474, 2019.

Reiser, F., Willmes, S., and Heinemann, G.: A New Algorithm for Daily Sea Ice Lead Identification in the Arctic and Antarctic Winter from Thermal-Infrared Satellite Imagery, Remote Sensing, 12, https://doi.org/10.3390/rs12121957, 2020.

Rheinlænder, J. W., Davy, R., Ólason, E., Rampal, P., Spensberger, C., Williams, T. D., Korosov, A., and Spengler, T.: Driving Mech-
590   anisms of an Extreme Winter Sea Ice Breakup Event in the Beaufort Sea, Geophysical Research Letters, 49, e2022GL099 024, https://doi.org/https://doi.org/10.1029/2022GL099024, 2022.

Ricker, R., Hendricks, S., Kaleschke, L., Tian-Kunze, X., King, J., and Haas, C.: A weekly Arctic sea-ice thickness data record from merged CryoSat–2 and SMOS satellite data, The Cryosphere, 11, 1607–1623, https://doi.org/10.5194/tc-11-1607-2017, 2017.

Ricker, R., Girard-Ardhuin, F., Krumpen, T., and Lique, C.: Satellite-derived sea ice export and its impact on Arctic ice mass balance, The
595   Cryosphere, 12, 3017–3032, https://doi.org/10.5194/tc-12-3017-2018, 2018.

Ricker, R., Kauker, F., Schweiger, A., Hendricks, S., Zhang, J., and Paul, S.: Evidence for an Increasing Role of Ocean Heat in Arctic Winter Sea Ice Growth, Journal of Climate, 34, 5215 – 5227, https://doi.org/10.1175/JCLI-D-20-0848.1, 2021.

Ringeisen, D., Tremblay, L. B., and Losch, M.: Non-normal flow rules affect fracture angles in sea ice viscous–plastic rheologies, The Cryosphere, 15, 2873–2888, https://doi.org/10.5194/tc-15-2873-2021, 2021.

600   Rousset, C., Vancoppenolle, M., Madec, G., Fichefet, T., Flavoni, S., Barthélemy, A., Benshila, R., Chanut, J., Lévy, C., Masson, S., et al.: The Louvain-La-Neuve sea ice model LIM3. 6: global and regional capabilities, Geoscientific Model Development, 8, 2991, 2015.

Schweiger, A., Lindsay, R., Zhang, J., Steele, M., Stern, H., and Kwok, R.: Uncertainty in modeled Arctic sea ice volume, Journal of Geophysical Research: Oceans, 116, https://doi.org/https://doi.org/10.1029/2011JC007084, 2011.

Semtner, A. J.: A Model for the Thermodynamic Growth of Sea Ice in Numerical Investigations of Climate, Journal of Physical Oceanogra-
605   phy, 6, 379 – 389, https://doi.org/10.1175/1520-0485(1976)006<0379:AMFTTG>2.0.CO;2, 1976.

Smedsrud, L. H., Halvorsen, M. H., Stroeve, J. C., Zhang, R., and Kloster, K.: Fram Strait sea ice export variability and September Arctic sea ice extent over the last 80 years, The Cryosphere, 11, 65–79, https://doi.org/10.5194/tc-11-65-2017, 2017.

Spall, M. A.: Dynamics and Thermodynamics of the Mean Transpolar Drift and Ice Thickness in the Arctic Ocean, Journal of Climate, 32, 8449–8463, https://doi.org/10.1175/JCLI-D-19-0252.1, 2019.

610   Spreen, G., Kern, S., Stammer, D., and Hansen, E.: Fram Strait sea ice volume export estimated between 2003 and 2008 from satellite data, Geophysical Research Letters, 36, https://doi.org/https://doi.org/10.1029/2009GL039591, 2009.

Spreen, G., de Steur, L., Divine, D., Gerland, S., Hansen, E., and Kwok, R.: Arctic Sea Ice Volume Export Through Fram Strait From 1992 to 2014, Journal of Geophysical Research: Oceans, 125, e2019JC016 039, https://doi.org/https://doi.org/10.1029/2019JC016039, e2019JC016039 10.1029/2019JC016039, 2020.

615   Steele, M., Zhang, J., Rothrock, D., and Stern, H.: The force balance of sea ice in a numerical model of the Arctic Ocean, Journal of Geophysical Research: Oceans, 102, 21 061–21 079, https://doi.org/https://doi.org/10.1029/97JC01454, 1997.

Steiner, N. S., Lee, W. G., and Christian, J. R.: Enhanced gas fluxes in small sea ice leads and cracks: Effects on CO_2 exchange and ocean acidification, Journal of Geophysical Research (Oceans), 118, 1195–1205, https://doi.org/10.1002/jgrc.20100, 2013.

Stroeve, J., Barrett, A., Serreze, M., and Schweiger, A.: Using records from submarine, aircraft and satellites to evaluate climate model
620   simulations of Arctic sea ice thickness, The Cryosphere, 8, 1839–1854, https://doi.org/10.5194/tc-8-1839-2014, 2014.

Strong, C. and Rigor, I. G.: Arctic marginal ice zone trending wider in summer and narrower in winter, Geophysical Research Letters, 40, 4864–4868, https://doi.org/10.1002/grl.50928, 2013.

Talandier, C. and Lique, C.: CREG025.L75-NEMO_r3.6.0: Source code as input files required to perform a CREG025.L75 experiment that relies on the NEMO release 3.6, https://doi.org/10.5281/zenodo.5802028, 2021.

625 Vinje, T., Nordlund, N., and Kvambekk, Å.: Monitoring ice thickness in Fram Strait, Journal of Geophysical Research: Oceans, 103, 10 437– 10 449, https://doi.org/https://doi.org/10.1029/97JC03360, 1998.

von Albedyll, L., Hendricks, S., Grodofzig, R., Krumpen, T., Arndt, S., Belter, H. J., Birnbaum, G., Cheng, B., Hoppmann, M., Hutchings, J., Itkin, P., Lei, R., Nicolaus, M., Ricker, R., Rohde, J., Suhrhoff, M., Timofeeva, A., Watkins, D., Webster, M., and Haas, C.: Thermodynamic and dynamic contributions to seasonal Arctic sea ice thickness distributions from airborne observations, Elementa: Science of the

630 Anthropocene, 10, https://doi.org/10.1525/elementa.2021.00074, 2022.

Walsh, J. E., Fetterer, F., Scott Stewart, J., and Chapman, W. L.: A database for depicting Arctic sea ice variations back to 1850, Geographical Review, 107, 89–107, https://doi.org/https://doi.org/10.1111/j.1931-0846.2016.12195.x, 2017.

Wang, Q., Danilov, S., Jung, T., Kaleschke, L., and Wernecke, A.: Sea ice leads in the Arctic Ocean: Model assessment, interannual variability and trends, Geophysical Research Letters, 43, 7019–7027, https://doi.org/https://doi.org/10.1002/2016GL068696, 2016.

635 Watts, M., Maslowski, W., Lee, Y. J., Kinney, J. C., and Osinski, R.: A Spatial Evaluation of Arctic Sea Ice and Regional Limitations in CMIP6 Historical Simulations, Journal of Climate, 34, 6399 – 6420, https://doi.org/10.1175/JCLI-D-20-0491.1, 2021.

Wilchinsky, A. V., Heorton, H. D. B. S., Feltham, D. L., and Holland, P. R.: Study of the Impact of Ice Formation in Leads upon the Sea Ice Pack Mass Balance Using a New Frazil and Grease Ice Parameterization, Journal of Physical Oceanography, 45, 2025 – 2047, https://doi.org/10.1175/JPO-D-14-0184.1, 2015.

640 Williams, T., Korosov, A., Rampal, P., and Ólason, E.: Presentation and evaluation of the Arctic sea ice forecasting system neXtSIM-F, The Cryosphere, 15, 3207–3227, https://doi.org/10.5194/tc-15-3207-2021, 2021.

Willmes, S. and Heinemann, G.: Sea-Ice Wintertime Lead Frequencies and Regional Characteristics in the Arctic, 2003–2015, Remote Sensing, 8, https://doi.org/10.3390/rs8010004, 2016.

Winton, M.: A Reformulated Three-Layer Sea Ice Model, Journal of Atmospheric and Oceanic Technology, 17, 525 – 531, 645 https://doi.org/10.1175/1520-0426(2000)017<0525:ARTLSI>2.0.CO;2, 2000.

WMO: WMO Sea-Ice Nomenclature, WMO, WMO, Geneva, 2014.

Zhang, J. and Rothrock, D. A.: Modeling Global Sea Ice with a Thickness and Enthalpy Distribution Model in Generalized Curvilinear Coordinates, Monthly Weather Review, 131, 845–861, https://doi.org/10.1175/1520-0493(2003)131<0845:mgsiwa>2.0.co;2, 2003.

Zhang, Y., Cheng, X., Liu, J., and Hui, F.: The potential of sea ice leads as a predictor for summer Arctic sea ice extent, The Cryosphere, 12, 650 3747–3757, https://doi.org/10.5194/tc-12-3747-2018, 2018.

Table 1. Main parameters used for the sea ice model in this study. All other parameters can be found in Olason et al. (2021a) (for the dynamics) and Rampal et al. (2019) (for the thermodynamics).

Parameter	symbol	former value (stand-alone)	new value (coupled)
Ice–atmosphere drag coefficient	C_a	2.0×10^{-3}	1.6×10^{-3}
Ice–ocean drag coefficient	C_w	5.5×10^{-3}	6.7×10^{-3}
Scaling parameter for the ridging threshold	P	$10 \text{ kPa/m}^{3/2}$	$3 \text{ kPa/m}^{3/2}$
Main model time step	Δt_m	900 s	450 s
Time step for sea ice dynamics solver	Δt	7.5 s	6 s
Maximum thickness of newly formed ice	$h_{\max}$	27.5 cm	18 cm
Sea ice albedo	a_{ice}	0.63	0.57
Snow albedo	a_{snow}	0.88	0.8
Critical thickness parameter for ice grounding	k_1	10	5
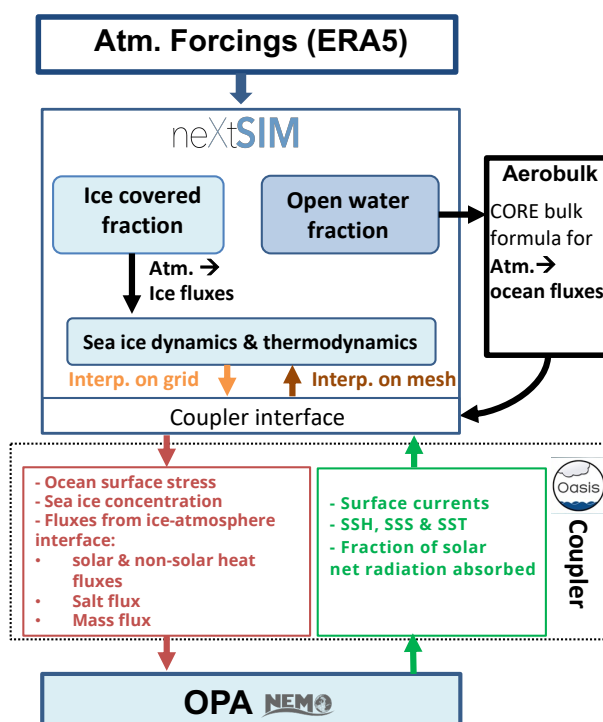
Figure 1. Summary of the coupling between neXtSIM and OPA, the ocean component of the NEMO modelling framework.
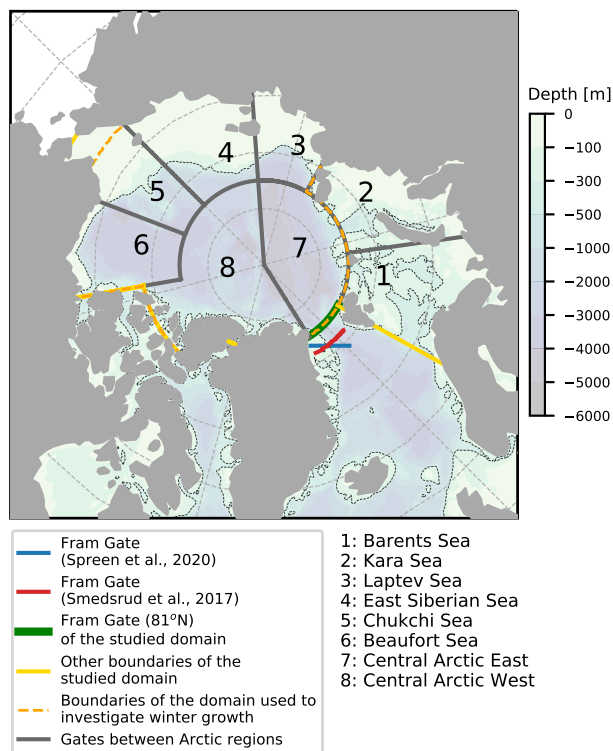
Figure 2. Domain, sub-domains and gates used for the analyses presented in this study.
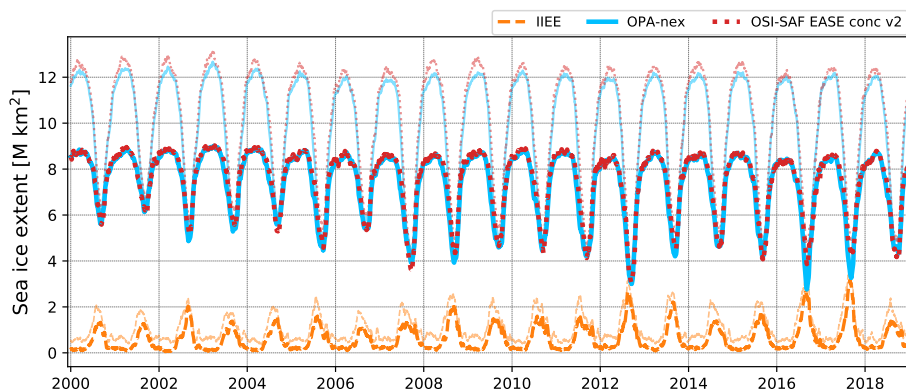
Figure 3. Time series of the sea ice extent for OPA-nex (in blue) compared to observations from the OSI-SAF EASE dataset (in red) for the study domain (bright lines) and for the whole domain model (faded lines). The orange dashed line represents the integrated ice-edge error (IIEE, Goessling et al., 2016) for the study domain (bright line) and for the whole domain (faded line).
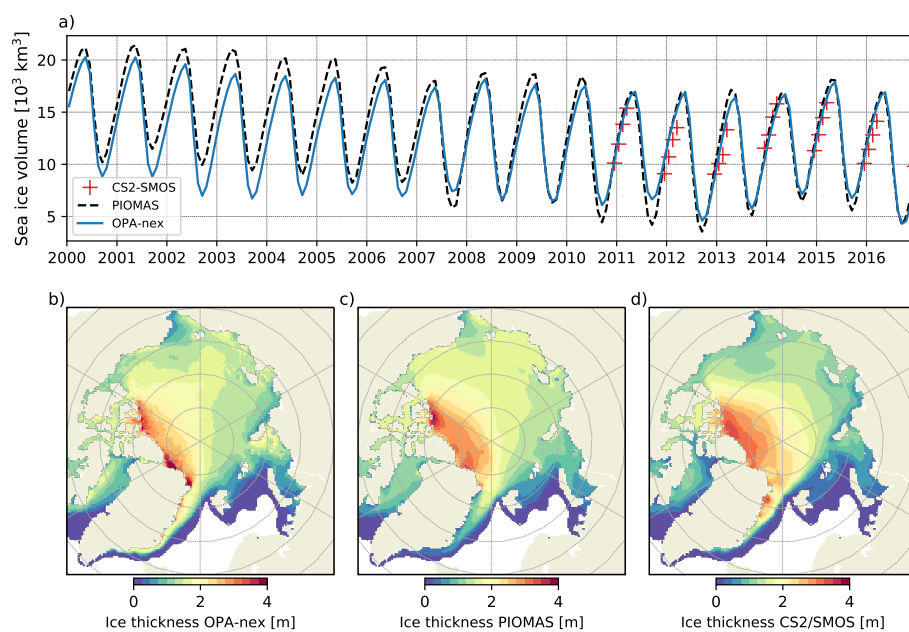
Figure 4. Time series of the monthly averaged sea ice volume (a) for OPA-nex compared to other reference datasets (PIOMAS and CS2SMOS). Panels (b, c, d) show a climatology of the sea ice thickness distribution in OPA-nex (b), the PIOMAS model (c) and the CS2SMOS dataset (d). This climatology is computed for the period from December to March over the years 2011–2018 (period of availability of the CS2SMOS product).
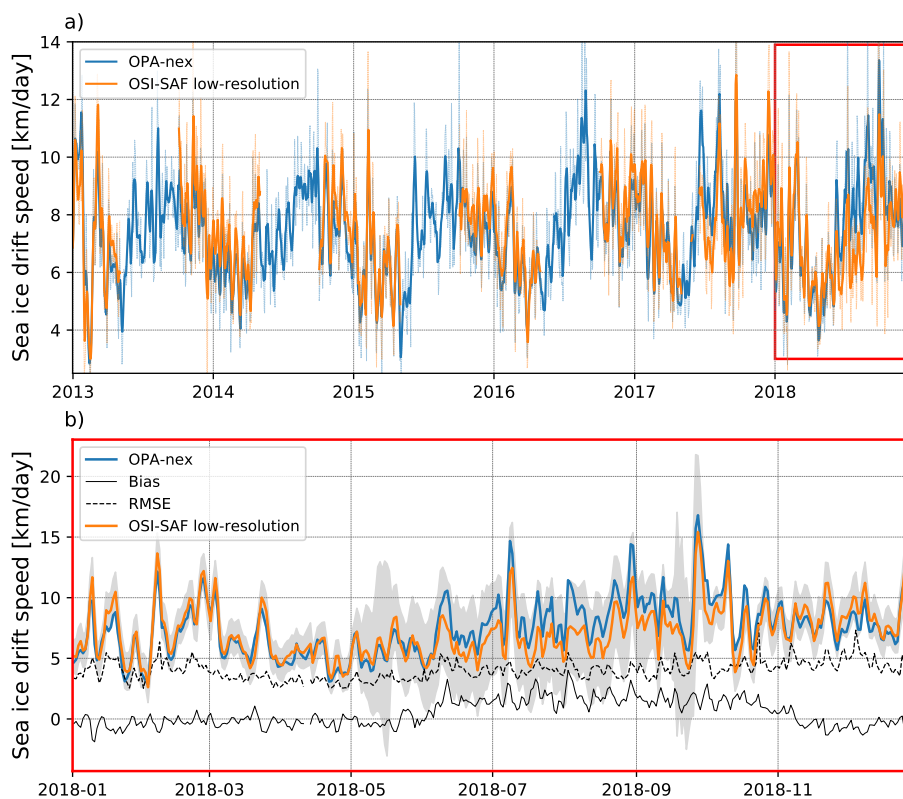
Figure 5. (a) Evolution of the spatially-averaged sea ice drift speed for OPA-nex (in blue) and the OSI-SAF low-resolution product (in orange). The OSI-SAF low-resolution product is available from 2010 onwards, but for the sake of readability we only show the period 2013–2018 . The thin lines correspond the daily values and the thick lines correspond to their associated 7-day running average. The red box in (a) delimits the time period over which we show a zoom on the daily values in (b). The solid and dashed black lines in (b) represent respectively the bias and the RMSE between OPA-nex and observations. The shaded area corresponds to the uncertainty of the observations (provided by OSI-SAF).
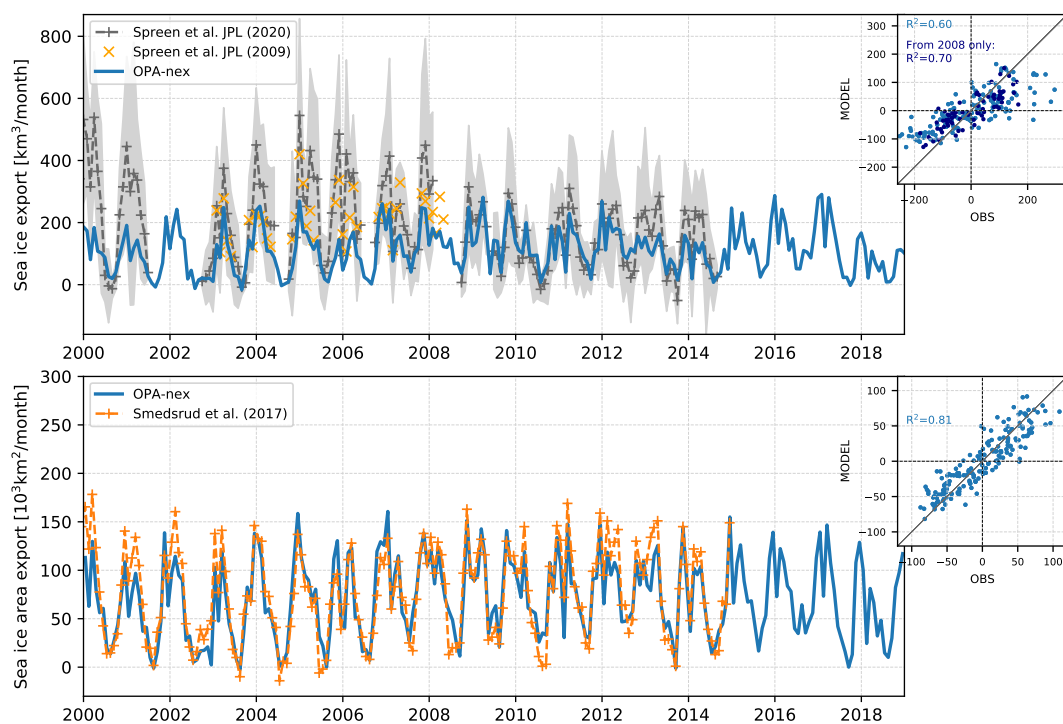
Figure 6. Top: Monthly sea ice volume export through Fram Strait (79°N) for the simulation (blue solid line) and as estimated by Spreen et al. (2020, grey dashed line) . The shaded area corresponds to the standard deviation based on daily transport values.

Bottom: Monthly sea ice area export through Fram Strait (79°N) for the simulation (blue solid line) and as estimated by Smedsrud et al. (2017) (orange dashed line). In the top right corner of each graph, the scatter plot shows the correlation between OPA-nex and the associated reference dataset after detrending both time series. R^2 correspond to the determination coefficient after 2008 only.
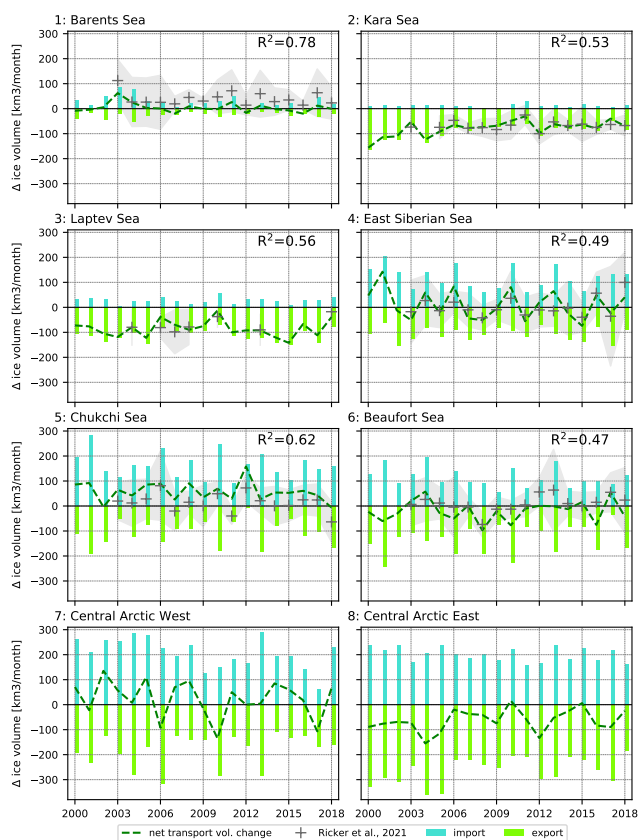
Figure 7. Temporal evolution of the sea ice mass balance due to dynamic processes. Results are presented region per region for the winter months (November to March) in OPA-nex (black dashed line) and compared to Ricker et al. (2021) estimations (grey plus signs). The contributions of sea ice export (green) versus import (turquoise) for each domain are also shown for each year. R values correspond to the correlation between detrended OPA-nex results and estimations from available observations over the period. Grey shaded areas correspond to the standard deviation of the satellite-derived retrievals for each winter season.
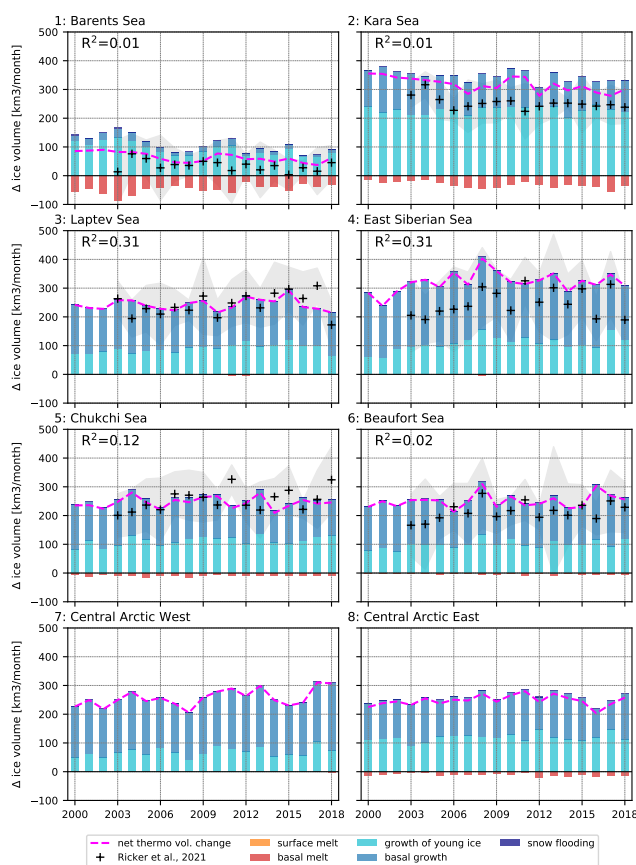
Figure 8. Temporal evolution of the sea ice mass balance due to thermodynamic processes. The net contribution of thermodynamics is represented by the dashed magenta line. Contributions from the different growth and melt processes for each year are also shown. Surface melt is not visible here as thickness data are only available for the freezing season. Results are presented region per region for the winter months (November to March) in OPA-nex and compared to Ricker et al. (2021) estimations. R^2 values correspond to the correlation between detrended model results and estimations from observations over the period of availability. Grey shaded areas correspond to the standard deviation of the satellite-derived retrievals for each winter season.
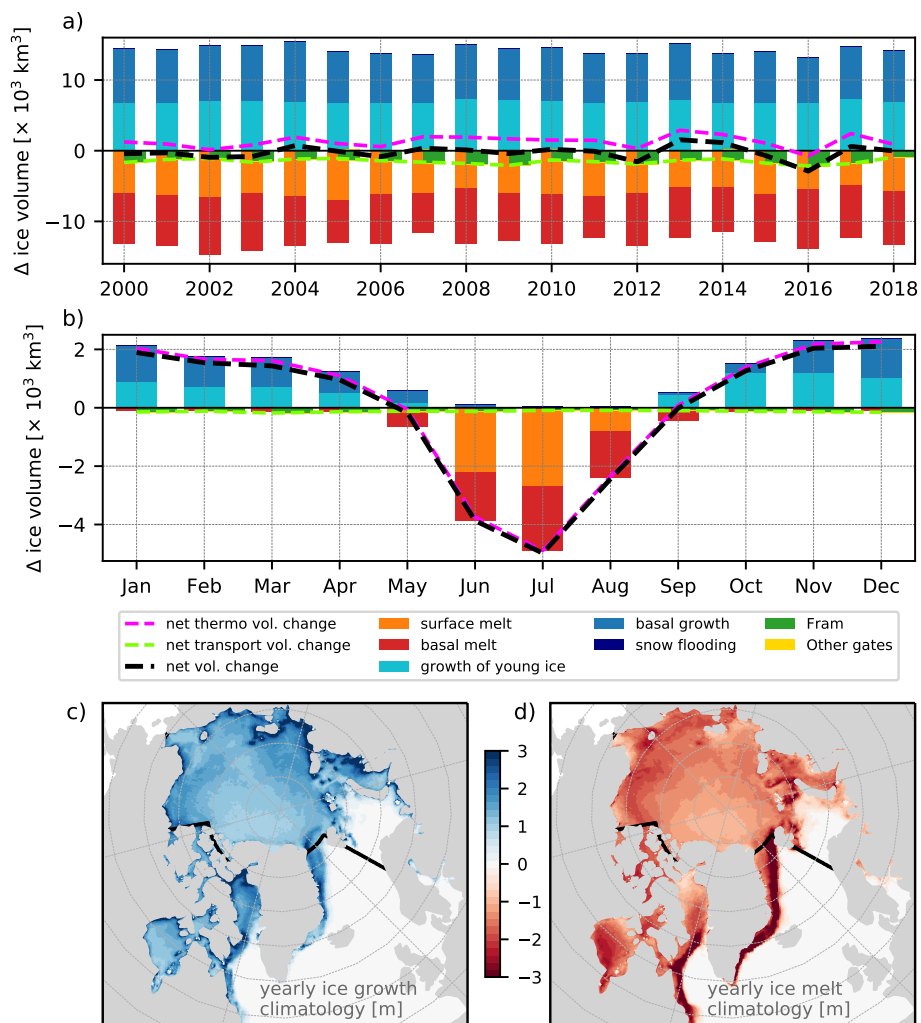
Figure 9. (a) Yearly evolution of the ice mass balance in OPA-nex distinguishing the different processes (thermodynamic and dynamic) contributing to ice volume gain/loss in the studied domain. (b) Monthly climatology of the ice mass balance over 2000–2018. Ice growth and melt distribution climatologies for these same periods are presented in panels (c) and (d) respectively.
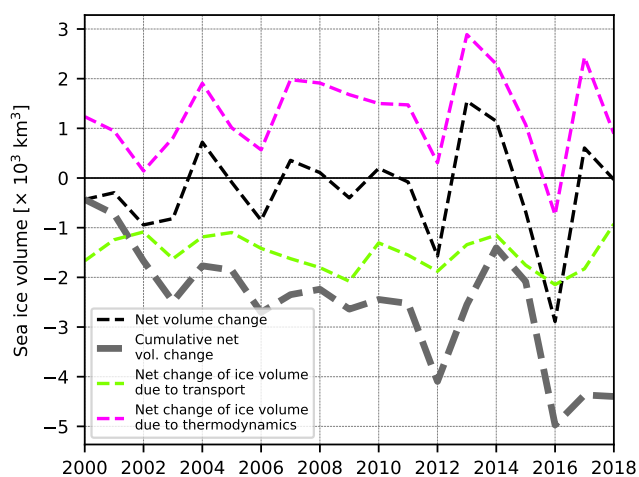
Figure 10. Temporal evolution of the yearly net sea ice volume change (dashed black line) and the cumulative yearly volume change (thick dashed grey line) over the period 2000–2018 within the study domain. The magenta and green lines represent the annual net volume change due to thermodynamic processes (magenta) and due to sea ice transport in/out of the domain (green line), as in Figure 9a.
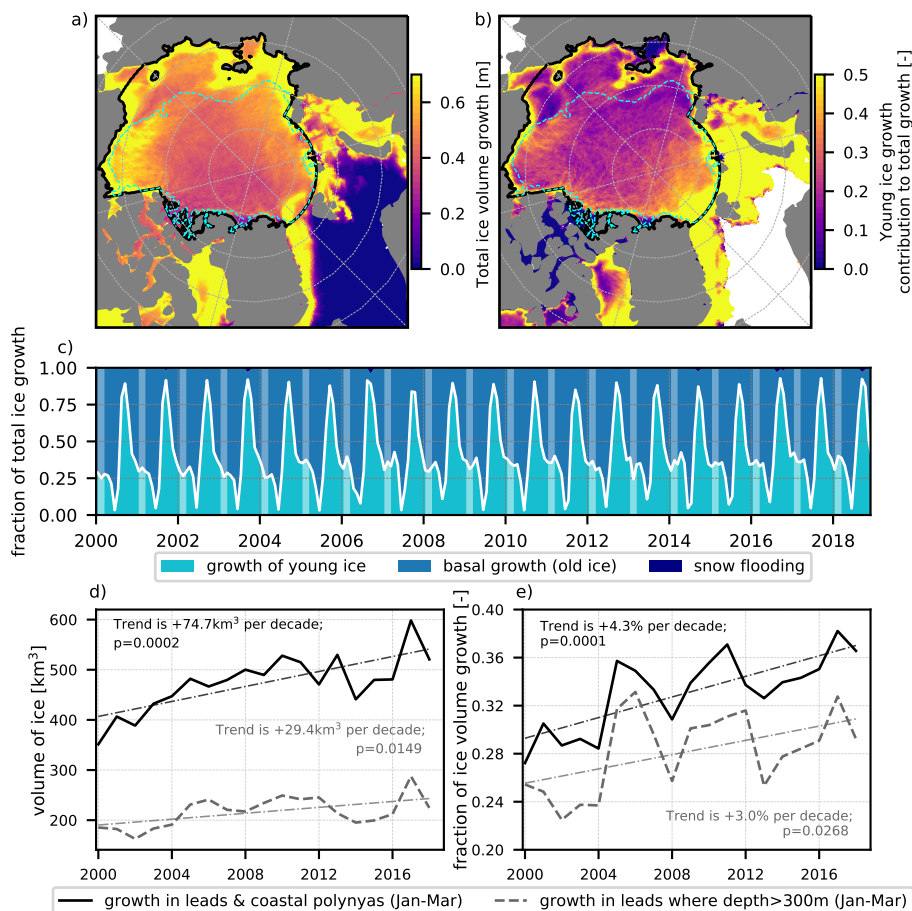
Figure 11. 2000–2018 climatology of the spatial distribution of ice volume (per area) growth in leads and polynyas in winter (a), and its contribution (ratio) to the total ice growth in winter (b). Panel (c) shows the evolution of this contribution compared to other ice growth processes over the period 2000–2018 within the domain delimited by the thick black solid line in panels (a,b). The temporal evolution of the integrated winter young ice volume growth and its contribution to total ice growth integrated over the domain are shown in panels (d,e) respectively (black solid lines). The grey dashed lines represent the same quantities, but for a sub-domain from which the regions shallower than 300m are excluded (cyan contour in panels a,b). We also display the trends associated with each line and their associated p-value.
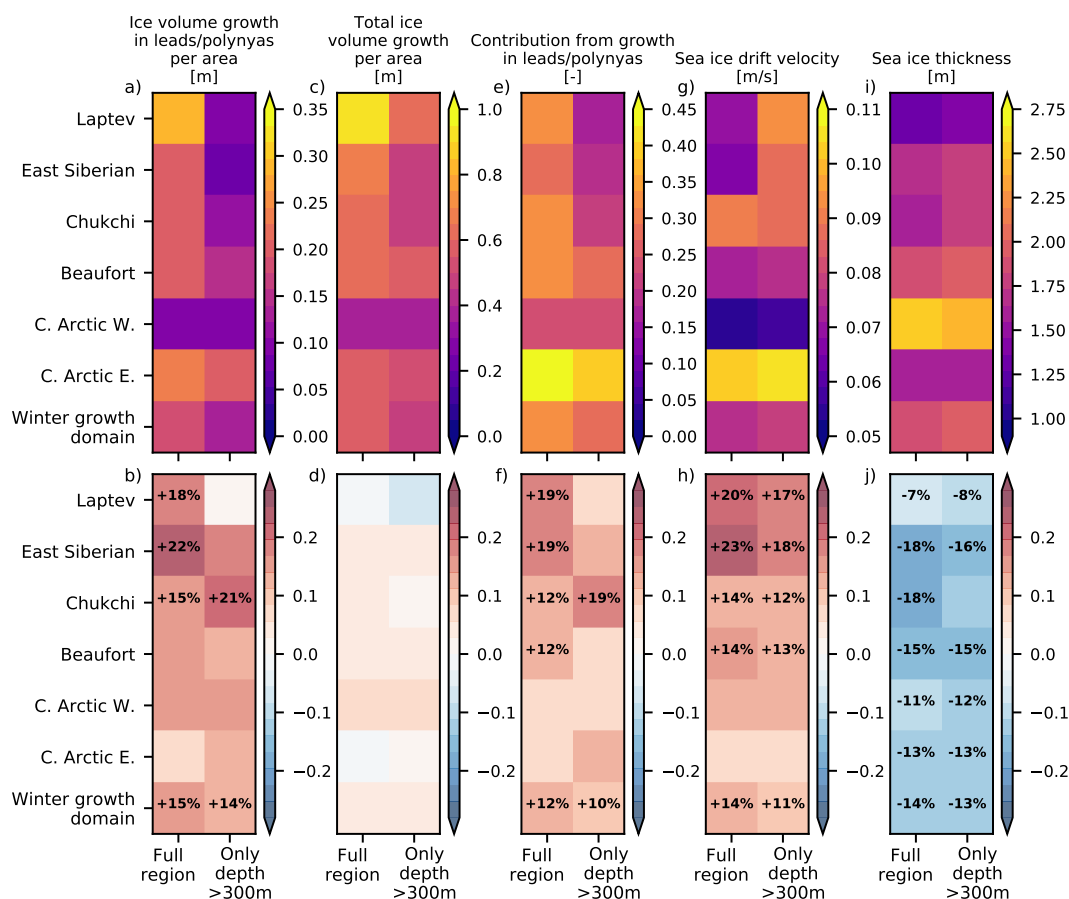
Figure 12. Top: Average quantities over the different sub-domains for, from left to right, winter ice volume growth in leads and polynyas, total winter ice growth, contribution of ice volume growth in leads and polynyas to total winter ice growth, sea ice drift velocity and thickness. Bottom: Trends over 2000–2018 in % (obtained by dividing the trend of each quantities by the mean values shown above) associated with each quantity. For each graph, the left column corresponds to the full sub-domains, and the right one only includes regions deeper than 300m.